31st International Conference
ENGINEERING MECHANICS 2025
Medlov, Czech Republic, May 12 –14, 2025
Paper **#46,** pp. 201–204, doi: 10.21495/em2025-201

ON DEM CONTACT MODEL FOR NON-SPHERICAL SOLIDS BUT CONSISTENT WITH HERTZ MODEL FOR SPHERES

Studeník O.[1], **Kotouč Šourek M.**[2], **Kočí P.**[3], **Isoz M.**[4]

Abstract: *To enable high-fidelity and physically relevant simulations of non-spherical suspensions, we aim to design a solver coupling computational fluid dynamics (CFD) with the discrete element method (DEM). The CFD part of the solver is based on the widely used OpenFOAM library. However, to design a robust and computationally efficient DEM for non-spherical particles is still an open problem, as the contact solution is, in this case, nontrivial. In this contribution, we propose an updated formulation of a DEM contact model for non-spherical particles that is (i) based on the concept of overlap volume, (ii) robust, and (iii) for the case of spheres, consistent with the standard Hertz-Mindlin model. The presented model is successfully verified against LIGGGHTS on a DEM benchmark test.*

Keywords: Dicrete Element Method (DEM), non-spherical solids, CFD-DEM, OpenFOAM.

1. Introduction

Suspension flows are abundant in both nature and industry, ranging from sand grains carried by the wind and riverbed movement to fluidized bed reactors and pharmaceutical microdosing. The diverse applications of such systems create demand for mathematical description. However, modeling dense suspensions requires complex computational approaches (Lin et al., 2020; Srinivasan et al., 2021). Particularly, coupling of computational fluid dynamics (CFD) with the discrete element method (DEM) can provide detailed insight into the behavior of coarse-grain dense suspensions (Lin et al., 2020). A crucial factor in such systems are particle collisions. A common approach is to assume spherical particles, which allows for an analytical and computationally efficient solution based on the Hertz-Mindlin model (Antypov and Elliott, 2010; Soltanbeigi et al., 2021). However, the particle shape plays a significant role (Xiong et al., 2021), introducing challenges in both (i) particle representation and (ii) contact modeling.

To address these challenges, different DEM approaches exist, including (i) the multi-sphere model, (ii) super-quadrics, and (iii) polyhedral representation (Zhong et al., 2016). The first two approaches leverage smooth and well defined surfaces, thus benefiting from the sphere contact model with minor adjustments. The polyhedral model is the most general approach and best suited for solids with sharp edges. At the same time, it requires a more advanced contact model, including additional estimations of geometric properties (Chen, 2012).

In this work, we present further developments of our in-house but open-source CFD-DEM library (Isoz et al., 2022). In particular, we describe a new modification of the contact model in DEM. The contact model is based on (Chen, 2012) but modified to be, for the case of spheres, consistent with the standard Hertz-Mindlin model. A test is designed to evaluate the repose angles of 1700 spherical particles, with results validated against the LIGGGHTS DEM solver (Kloss et al., 2012).

[1] Ing. Ondřej Studeník: Institute of Thermomechanics, Czech Academy of Sciences (CAS), Dolejškova 1402/5; 182 00 Prague; CZ and Department of Chemical Engineering, University of Chemistry and Technology (UCT), Technická 5; 166 28 Prague; CZ
[2] Ing. Martin Kotouč Šourek: Department of Chemical Engineering, UCT, Technická 5; 166 28 Prague; CZ
[3] Prof. Ing. Petr Kočí, Ph.D.: Department of Chemical Engineering, UCT, Technická 5; 166 28 Prague; CZ
[4] Ing. Martin Isoz, Ph.D.: Institute of Thermomechanics, CAS, Dolejškova 1402/5; 182 00, Prague; CZ and Department of Mathematics, Informatics, and Cybernetics, UCT, Technická 5; 166 28 Prague; CZ,e-mail: isozm@it.cas.cz

2. Framework fundamentals

Particle definition Fundamental features of the presented DEM solver are its direct embedding in the CFD code and focus on non-spherical particles. The shape of the particle $\mathcal{B}_i$ is described using a triangulated surface mesh $\partial\mathcal{B}_i$. During program execution, $\partial\mathcal{B}_i$ is kept in computer memory and undergoes a rigid solid body motion governed by Newton's second law. Besides its shape, each particle has its material properties, such as the density ρ, Poisson ratio ν, Young's and Shear moduli Y, G, and the friction coefficient μ, which are assumed constant and homogeneous.

Next, to estimate geometrical properties, such as particle mass m_i, center of gravity, or moment of inertia I_i, the solver creates a projection of the body $\mathcal{B}_i$ on a finite volume (FV) mesh Ω^h, which is provided by the CFD part of the code. The projection is carried out using a color function λ, which is defined on the FV mesh and returns the solid volume fraction for each FV cell.

Movement of the particles As stated above, the movement of $\mathcal{B}_i$ is governed by Newton's second law of motion,

$$m_i \frac{\mathrm{d}^2 \boldsymbol{x}_i}{\mathrm{d}t^2} = \boldsymbol{f}_i^{\mathrm{g}} + \boldsymbol{f}_i^{\mathrm{c}} + \boldsymbol{f}_i^{\mathrm{d}}, \quad I_i \frac{\mathrm{d}\boldsymbol{\omega}_i}{\mathrm{d}t} = \boldsymbol{t}_i^{\mathrm{c}} + \boldsymbol{t}_i^{\mathrm{d}}\,. \tag{1}$$

Here, the position $\boldsymbol{x}_i$ of $\mathcal{B}_i$ and its angular velocity $\boldsymbol{\omega}_i$ are estimated based on the influence of forces $\boldsymbol{f}$ and torques $\boldsymbol{t}$. The forces and torques considered are gravity/buoyancy (g), collisions (c), and drag (d) at a given time t. The drag force is considered only for CFD-DEM applications and will be neglected hereafter. The equations are solved in a finite difference manner while assuming that the forces and torques are constant during each time step Δt, see (Studeník et al., 2024).

Collision force Out of all considered sources in governing equations, the collision term is probably the most significant with respect to the overall behavior of systems of interest. There are many approaches to its solution. The considered solver builds on the *soft* -DEM approach, which enables particle overlap as a way to replace the elastic or elasto-plastic deformations at the contact point, compensating for the rigid nature of the simulated solids. The first approach to model such forces was derived for the spherical particles using the magnitude of the overlap to scale the contact force. According to the Hertz-Mindlin model (Soltanbeigi et al., 2021; Antypov and Elliott, 2010), which is constructed as a spring-dashpot model. Its formulation for the normal component of the contact force can be written as

$$\boldsymbol{f}^{\mathrm{c,n}} = \left(k^{\mathrm{n}}\delta + \gamma\sqrt{k^{\mathrm{n}} M^{\mathrm{red}}}\,\frac{\mathrm{d}\delta}{\mathrm{d}t} \right) \boldsymbol{n}^{\mathrm{c}}\,, \quad k^{\mathrm{n}} = \frac{4}{3} Y^{\mathrm{red}} \sqrt{r^{\mathrm{red}}\delta}, \quad \gamma = \frac{-\sqrt{5}\ln(\varepsilon)}{\sqrt{\ln(\varepsilon)^2 + \pi^2}}\,, \tag{2}$$

with k^{n} denoting the elastic stiffness derived from reduced material properties and particle overlap length δ. Please note that the superscript red denotes the harmonically averaged (reduced) properties weighted by the Poisson ratio for the cases of Y and G. The dissipation of energy during the collision is accounted for by the damping factor γ, based on the restitution coefficient ε. The contact normal $\boldsymbol{n}^{\mathrm{c}}$ and overlap δ for spherical particles are

$$\delta = \max\left[0, (r_i + r_j) - (\boldsymbol{x}_i - \boldsymbol{x}_j)\cdot \boldsymbol{n}^{\mathrm{c}}\right], \quad \boldsymbol{n}^{\mathrm{c}} = \frac{\boldsymbol{x}_i - \boldsymbol{x}_j}{||\boldsymbol{x}_i - \boldsymbol{x}_j||}\,, \tag{3}$$

where $\boldsymbol{x}$ and r are the respective positions and radii of spheres forming the colliding pair. The increment to tangential component to the contact force can be formulated as,

$$\Delta\boldsymbol{f}^{\mathrm{c,t}} = k^{\mathrm{t}}\,\boldsymbol{u}_{\mathrm{r}}^{\mathrm{t}}\,\Delta t, -2\gamma^{\mathrm{n}}\sqrt{k^{\mathrm{t}} M^{\mathrm{red}}}\,\boldsymbol{u}_{\mathrm{r}}^{\mathrm{t}}, \quad k^{\mathrm{t}} = 8\,G^{\mathrm{red}}\sqrt{r^{\mathrm{red}}\delta}\,, \quad \boldsymbol{u}_{\mathrm{r}}^{\mathrm{t}} = \boldsymbol{u}_{\mathrm{r}} - (\boldsymbol{u}_{\mathrm{r}}\cdot\boldsymbol{n}^{\mathrm{c}})\,\boldsymbol{n}^{\mathrm{c}}\,, \tag{4}$$

where k^{t} is a tangential elastic stiffness and $\boldsymbol{u}_{\mathrm{r}}^{\mathrm{t}}$ is a tangential component of the relative velocity to the contact pair, with the complete form given as $\boldsymbol{u}_{\mathrm{r}} = \boldsymbol{u}_i - \boldsymbol{u}_j + (\boldsymbol{\omega}_i \times \boldsymbol{\ell}_i - \boldsymbol{\omega}_j \times \boldsymbol{\ell}_j)$. In addition, the tangential force is treated with respect to the contact history, and the value of the last iteration $\Delta\boldsymbol{f}_{\mathrm{old}}^{\mathrm{c,t}}$ is rescaled and reprojected to account for the new iteration. The new tangential force then consists of the former value and the current increase $\Delta\boldsymbol{f}^{\mathrm{c,t}}$. However, to account for surface friction, the estimated tangential force is subsequently corrected with Coulomb's Law as

$$\boldsymbol{f}_{\mathrm{new}}^{\mathrm{c,t}} = \Delta\boldsymbol{f}_{\mathrm{old}}^{\mathrm{c,t}} + \Delta\boldsymbol{f}^{\mathrm{c,t}} \quad \boldsymbol{f}^{\mathrm{c,t}} = \min\left(\left\|\boldsymbol{f}_{\mathrm{new}}^{\mathrm{c,t}}\right\|, \mu\left\|\boldsymbol{f}^{\mathrm{c,n}}\right\|\right) \frac{\boldsymbol{f}_{\mathrm{new}}^{\mathrm{c,t}}}{\left\|\boldsymbol{f}_{\mathrm{new}}^{\mathrm{c,t}}\right\|}\,. \tag{5}$$

Consequently, the evaluated components are combined as $\boldsymbol{f}^{\mathrm{c}} = \boldsymbol{f}^{\mathrm{c,n}} + \boldsymbol{f}^{\mathrm{c,t}}$. The resulting contact force is added to the governing equations (1), for each particle of the colliding pair $i - j$ as $\boldsymbol{f}_i^{\mathrm{c}} = \boldsymbol{f}^{\mathrm{c}}$, $\boldsymbol{f}_j^{\mathrm{c}} = -\boldsymbol{f}^{\mathrm{c}}$ and $\boldsymbol{t}_i^{\mathrm{c}} = \boldsymbol{r}_i \times \boldsymbol{f}^{\mathrm{c}}$, $\boldsymbol{t}_j^{\mathrm{c}} = \boldsymbol{r}_j \times (-\boldsymbol{f}^{\mathrm{c}})$ for force and torques, respectively.

The approach to contact treatment described above is restricted to spherical particles and is applied in DEM solvers such as LIGGGHTS (Kloss et al., 2012) or MUSEN (Dosta and Skorych, 2020). Although there are many approaches using some sort of characteristic overlap length for non-spherical solids, none of these approaches is currently dominant in the research community.

In this contribution, we build on the approach first presented in (Chen, 2012), where the particle overlap is characterized using directly its volume V^{o} rather than through conversion of V^{o} to some characteristic overlap length. Therefore, a new formulation for contact force treatment was introduced in the original publication (Chen, 2012). The main difference compared to the Hertz-Mindlin model is best visible for the normal component of contact force,

$$\boldsymbol{f}^{\mathrm{c,n}} = \left(\frac{Y^{\mathrm{red}}\, V^{\mathrm{o}}}{\ell^{\mathrm{c}}} + \gamma^* \sqrt{\frac{Y^{\mathrm{red}}\, M^{\mathrm{red}}}{(\ell^{\mathrm{c}})^3}} \frac{\mathrm{d}\, V^{\mathrm{o}}}{\mathrm{d}\, t} \right) \boldsymbol{n}^{\mathrm{c}},\ \ell^{\mathrm{c}} = 4 \frac{\|\boldsymbol{\ell}_j\|\ \|\boldsymbol{\ell}_i\|}{\|\boldsymbol{\ell}_j\| + \|\boldsymbol{\ell}_i\|},\ \frac{\mathrm{d}V^{\mathrm{o}}}{\mathrm{d}t} = \bar{A}^{\mathrm{c}} \left(\boldsymbol{u}_{\mathrm{r}} \cdot \boldsymbol{n}^{\mathrm{c}} \right) , \tag{6}$$

where ℓ^{c} stands for the characteristic length scale of the contact given by the distances $\|\boldsymbol{\ell}\|$ between the contact center and the centroids of the respective bodies. The time derivative of the overlap volume might be simplified with the assumption of a constant contact cross-sectional area $\bar{A}^{\mathrm{c}}$ multiplied by the relative velocity to account for the temporal change.

Please note that the model (6) was derived in (Chen, 2012) for rectangular particles with the objective to study wave propagation in an array of such particles. However, the model can be further modified to take into account various particle shapes. In particular, the shape-dependent parameter in (6) is the constant 4 in the definition of ℓ^{c}. In the generalization, a new effective curvature parameter C_ℓ is applied, for which the values $C_\ell = 4$ account for a flat surface and $C_\ell = 0.55$ for spheres. Combining (2) and (6) and pluging in C_ℓ, the overall model might be rewritten as follows

$$\boldsymbol{f}^{\mathrm{c,n}} = \left(k_*^{\mathrm{n}} \delta^{\mathrm{o}} + \gamma^{\mathrm{n}} \sqrt{k_*^{\mathrm{n}} M^{\mathrm{red}}}\, \boldsymbol{u}_{\mathrm{r}} \cdot \boldsymbol{n}^{\mathrm{c}} \right) \boldsymbol{n}^{\mathrm{c}} ,\ k_*^{\mathrm{n}} = Y^{\mathrm{red}} \frac{\bar{A}^{\mathrm{c}}}{\ell^{\mathrm{c}}} ,\ \ell^{\mathrm{c}} = C_\ell \frac{\|\boldsymbol{\ell}_j\|\ \|\boldsymbol{\ell}_i\|}{\|\boldsymbol{\ell}_j\| + \|\boldsymbol{\ell}_i\|} . \tag{7}$$

In (7), k_*^{n} is the effective stiffness of the material for the volume-defined contact, $\delta^{\mathrm{o}} = V^{\mathrm{o}} / \bar{A}^{\mathrm{c}}$ is derived from the overlap volume and the contact cross-section area. These modifications to the original model (6) have proven quite effective and were applied to tangential forces only with the change of the constant for the tangential elastic stiffness given as $k_*^{\mathrm{t}} = 8\, G^{\mathrm{red}} \bar{A}^{\mathrm{c}} / \ell^{\mathrm{c}}$. The updated contact model was first presented in (Studeník et al., 2024). and the reader is referred to this work for details regarding the implementation and verification tests of the solver.

3. Results

To further verify the updated implementation of the contact model, we focus on the scaled-up application rather than on single collision events, which are summarized in (Studeník et al., 2024). The application considered in this contribution is a simulation study on the influence of friction coefficient on repose angle, with the result of comparing the presented solver to the results from the LIGGGHTS DEM solver.

The study is set with the poured column of 1700 monodispersed spheres with diameter $d = 2.5\,\mathrm{cm}$ and density $\rho = 2650\,\mathrm{kg/m^3}$. Each particle is prescribed with the properties of the material as $Y = 500\,\mathrm{MPa}$, $\nu = 0.4$, $\varepsilon = 0.15$. Gravity is considered as $\boldsymbol{g} = (0, -9.81, 0)^{\mathrm{T}}\,\mathrm{m/s^2}$.The controlled variable is the friction coefficient set to $\mu = 0,\ 0.3,\ 1.0$. The integration step is fixed on the value of $\Delta t = 10^{-6}\,\mathrm{s}$ with simulation time of $2\,\mathrm{s}$. The results are summarized. in Fig. 1 showing the increasing value of the repose angle $\tilde{\alpha}$. The results show a discrepancy with the general rule of thumb for the repose angle given as $\tan(\tilde{\alpha}) = \mu$. This might be due to several factors, including an overestimated dissipation coefficient, non-realistic particle distribution, or an unfitting method to estimate the repose angle value. The last cause mentioned has the highest probability. For this study, we employed a simple image analysis method. For the presentation of our results at the conference, we will include more advanced results using the algorithm proposed in (Müller et al., 2021). Nevertheless, the results show good agreement with the LIGGGHTS-DEM solver, verifying the updated contact model for further applications.

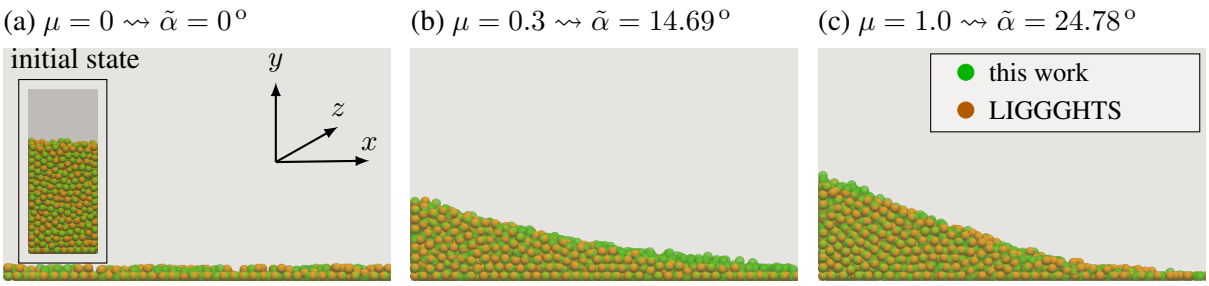

Fig. 1: Results of repose angle ($\tilde{\alpha}$) study, displayed as overlay of end time $t = 2\,\mathrm{s}$ for the two tested solvers and three different friction coefficients (μ).

4. Conclusions

In this contribution, we present the updated contact force formulation for both normal and tangential components while comparing it to the standard *soft*-DEM implementation of the Hertz-Mindlin model. Furthermore, the results of the given implementation are verified against the LIGGGHTS DEM solver for the estimation of the repose angle, which shows general good agreement. In the presentation of this contribution we will extend the results listed here with new postprocessing methods and add the results for studies using polyheadron-based solids, both convex and non-convex.

The basic configuration for the test presented and full software library are available from the GitHub repository github.com/techMathGroup/openHFDIB-DEM and available for OpenFOAMv8 with a port to OpenFOAMv2406 being prepared.

Acknowledgments

This research was co-funded by the European Union under the project Metamaterials for thermally stressed machine components (reg. no. CZ.02.01.01/00/23_020/0008501). The work was financially supported by the institutional support RVO:61388998, by the grant project with No. 25-17815S of the Czech Science Foundation of the Czech Republic and by the grant project with No. TN02000069/001N of the Technology Agency of the Czech Republic,.

References

Antypov, D. and Elliott, J. A. (2010) On an analytical solution for the damped hertzian spring. *Europhysics Letters*, 94.

Chen, J. (2012) *Understanding the Discrete Element Method: Simulation of Non-Spherical Particles for Granular and Multi-Body Systems*. PhD thesis.

Dosta, M. and Skorych, V. (2020) MUSEN: An open-source framework for GPU-accelerated DEM simulations. *SoftwareX*, 12, pp. 100618.

Isoz, M., Kotouč Šourek, M., Studeník, O., and Kočí, P. (2022) Hybrid fictitious domain-immersed boundary solver coupled with discrete element method for simulations of flows laden with arbitrarily-shaped particles. *Computers and Fluids*, 244, pp. 105538.

Kloss, C., Goniva, C., Hager, A., Amberger, S., and S.Pirker (2012) Models, algorithms and validation for opensource DEM and CFD–DEM. *Progress in Computational Fluid Dynamics, an International Journal*, 12, pp. 140–152.

Lin, J., Luo, K., Wang, S., Hu, C., and Fan, J. (2020) An augmented coarse-grained cfd-dem approach for simulation of fluidized beds. *Advanced Powder Technology*, 31, 10, pp. 4420–4427.

Müller, D., Fimbinger, E., and Brand, C. (2021) Algorithm for the determination of the angle of repose in bulk material analysis. *Powder Technology*, 383, pp. 598–605.

Soltanbeigi, B., Podlozhnyuk, A., Kloss, C., S. Pirker, J. Y. O., and Papanicolopulos, S. (2021) Influence of various dem shape representation methods on packing and shearing of granular assemblies. *Granular Matter*, 26.

Srinivasan, S., Van den Akker, H. E., and Shardt, O. (2021) Numerical simulations of dense granular suspensions in laminar flow under constant and varying shear rates. *Computers and Fluids*, 230, pp. 105115.

Studeník, O., Isoz, M., Kotouč Šourek, M., and Kočí, P. (2024) OpenHFDIB-DEM: An extension to OpenFOAM for CFD-DEM simulations with arbitrary particle shapes. *SoftwareX*, 27.

Xiong, H., Wu, H., Bao, X., and Fei, J. (2021) Investigating effect of particle shape on suffusion by cfd-dem modeling. *Construction and Building Materials*, 289, pp. 123043.

Zhong, W., Yu, A., Liu, X., Tong, Z., and Zhang, H. (2016) DEM/CFD-DEM modelling of non-spherical particulate systems: Theoretical developments and applications. *Powder Technology*, 302, pp. 108–152.